

# Supplementary Information for "Attosecond lighthouses from plasma mirrors"

Jonathan A. Wheeler<sup>1,\*</sup>, Antonin Borot<sup>1,\*</sup>, Sylvain Monchocé<sup>2</sup>, Henri Vincenti<sup>2</sup>, Aurelien Ricci<sup>1,3</sup>, Arnaud Malvache<sup>1</sup>, Rodrigo Lopez-Martens<sup>1,†</sup>, and Fabien Quéré<sup>2,†</sup>

<sup>1</sup>Laboratoire d'Optique Appliquée, ENSTA-Paristech, Ecole Polytechnique, CNRS, 91761 Palaiseau, France,

<sup>2</sup>Service des Photons, Atomes et Molécules, CEA, DSM/IRAMIS, CEN Saclay, 91191 Gif-sur-Yvette, France,

<sup>3</sup>Laser Solutions Unit, Thales Optronique SA, 78990 Elancourt, France

## S1 Experiment

Figure S1 shows a sketch of the experimental set-up, including the diagnostics used in the characterization of the near-infrared (NIR) and extreme ultraviolet (EUV) pulses. The experimental chamber layout is shown in Fig. S1a, while b & c display the NIR imaging spectrometer and EUV spectrometer, respectively. To accommodate the vertical sampling capabilities of both the NIR and EUV spectrometers while maintaining the polarization relative to the target surface required for CWE, the angular dispersion was induced along the vertical axis of a  $p$ -polarized beam. As opposed to the simplified sketch of the experiment presented in Fig. 2 of the paper, the prisms are actually arranged in a horizontal orientation (for reasons of laser safety and convenience) with an angle relative to the  $p$ -polarized beam to minimize surface losses. Thus both the angular dispersion and polarization are naturally along the horizontal axis of the beam. To rotate the direction of angular dispersion to the vertical axis while keeping the  $p$  polarization, two steps are taken. First, a broadband half-waveplate rotates the polarization to  $s$ -configuration with no affect on the angular dispersion. Then a crossed periscope that delivers the source from the optical table to the experimental chamber is used to rotate the beam so that both the polarization and the angular dispersion are in the desired orientation—horizontal and vertical respectively. This configuration eventually leads to a vertical spread of the EUV spatial beam profile.

The first diagnostic shown in Fig. S1b measures the NIR spatial chirp at focus. It can be monitored under vacuum by removing the solid target and imaging the focus of the beam with a microscope objective into an imaging NIR spectrometer, which gives the spectrum at focus along the vertical direction. Assuming flat spectral and spatial phase, this measurement leads to an immediate estimate of the wavefront rotation velocity during the experiment.

Two diagnostics characterize the EUV pulses reflected from the plasma mirror. The first is pictured in Fig. 2 of the main paper and is a bare two-stage MCP with integrated phosphor screen placed in

\*These authors contributed equally to this work.

†Corresponding authors: rodrigo.lopez-martens@ensta-paristech.fr and fabien.quere@cea.fr

the path of the plasma reflection 20-cm from the target and allows for direct imaging of the spatial profile of the EUV beam. Note that the photon energy response of the MCP directly filters out photon energies below H7 ( $\approx 11$  eV), such that the measured spatial profile results from the superposition of all photon energies above this cut-off. The second diagnostic is an EUV spectrometer shown in Fig. S1c that samples a limited central portion of the attosecond pulses due to acceptance angles of  $0.335^\circ$  and  $2.45^\circ$  in the horizontal and vertical axes respectively. The spectrometer consists of an aberration-corrected concave grating (Hitachi 001-0639, 600 g/mm) that diffracts the beam into the horizontal plane. The vertical axis is non-imaging and gives access to the divergence of the spectral components of the sampled portion of the beam. The spectral measurement presented in Fig. 3 of the main paper are obtained by taking a lineout of the spectrum from the center of the MCP detector (see Fig. S1c)

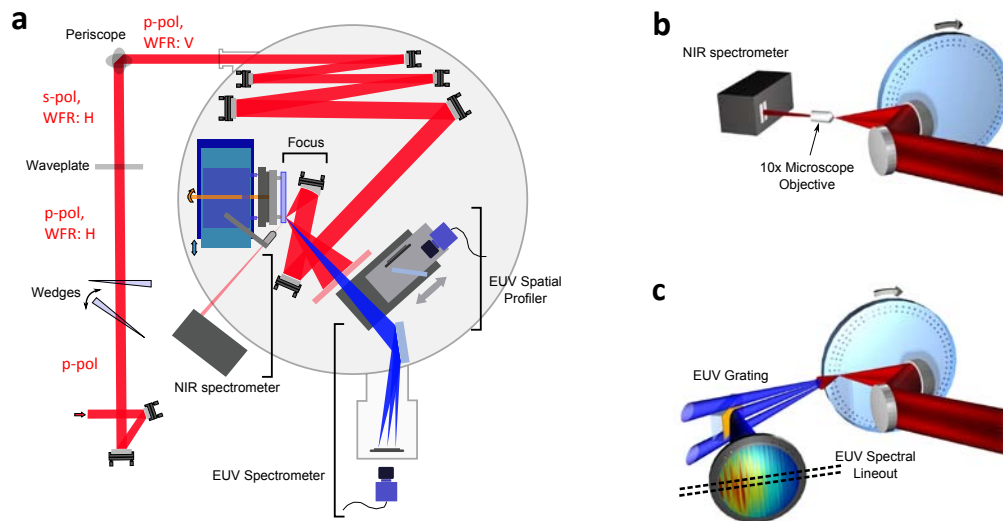


**Figure S1: Schematic of the experiment.** **a**, The overall experimental chamber layout showing the target and all three diagnostics. In **b** the removal of the target allows for the imaging of the laser beam focus to be coupled into an imaging optical spectrometer and gives the spatially-resolved laser spectrum at focus. The EUV spatial profile diagnostic is shown in Fig. 2 of the main paper, while in **c** the spectral measurements are made by removing the spatial profile MCP detector which allows a central portion of the beam to be measured by an EUV spectrometer with angular resolution in the vertical direction. The dashed lines highlight the central region sampled by the spectral line-outs given in the paper.

## S2 Spectral oscillations of isolated attosecond pulses

Of concern are the additional high-frequency oscillations within the EUV spectra shown in the last column of Fig. 3 in the paper and are particularly visible in the bottom right image corresponding to the case of an isolated attosecond pulse. An inverse Fourier analysis of this spectrum shows that these modulations correspond to a peak around 12 fs in the time domain and suggests the presence of either a pre- or post- EUV burst at this delay from the main attosecond EUV pulse. However, these spectral modulations have a low contrast  $C$  which averages to 12% across the entire EUV spectrum, ranging from a maximum of 20% at the lowest energies and decreasing at higher energies. This pre

or post-pulse is therefore extremely weak, with an energy of about  $C^2/4 \approx 0.4\%$  that of the main attosecond pulse.

This secondary EUV burst is likely due to CWE induced by a weak satellite of the main driving laser pulse. This interpretation is supported by a temporal reconstruction of the driving laser pulse using FROG (see Fig. S2). Indeed, this reconstruction gives a pulse duration of 6.9 fs, and exhibits a satellite pulse roughly 12 fs away from the main peak (with an ambiguity as to whether it is a pre-pulse or post-pulse due to the nature of the SHG-FROG).

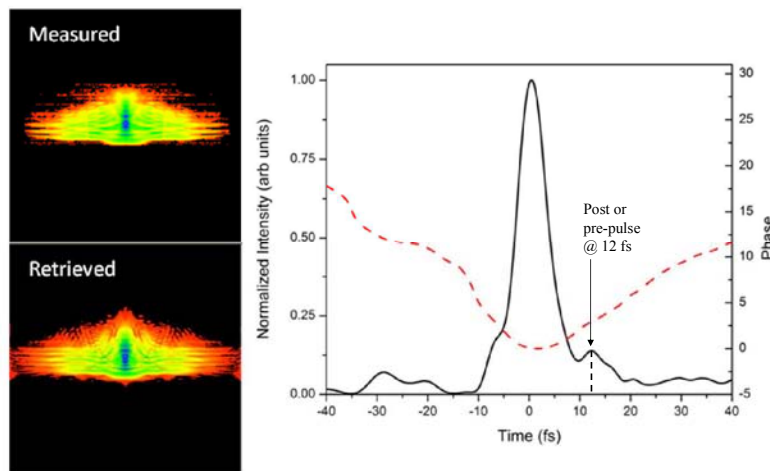


**Figure S2: SHG-FROG of infrared pulse.** The retrieved results of the SHG-FROG used to measure the pulse duration delivered to the experimental chamber. Here the compressed pulse with aligned prisms is measured to have a duration of 6.9 fs. The retrieved pulse shows a shoulder at approximately 12 fs away from its peak.

However, this interpretation raises a problem: if this EUV emission is shifted in time by 12 fs, the time-to-space mapping that results from the WFR should induce a large angular shift between the secondary EUV beam and the main EUV beamlets, resulting in no spatial overlap, and thus no interferences between the two. The answer to this is still not completely clarified, as it would require a complete knowledge of the laser field both in space and time. One possible explanation is that the WFR at focus is only apparent near the point of optimal temporal compression for the laser pulse. Because the satellite infrared pulse is an unoptimized artifact of the laser system, it is likely that it may have sufficient energy to generate an EUV signal without being adequately compressed to exhibit significant WFR. In such a case, the time-to-space mapping would not apply to the weak EUV beam emitted by this temporal satellite and it would remain reflected colinear to the central peak of the EUV beamlet profile in the direction of the EUV spectrometer.

### S3 Particle-In-Cell simulations of experimental conditions.

To support our conclusion that each beamlet of Figs. 3c and 4 consists of an isolated attosecond pulse, we have used the CALDER code to perform 2D particle-in-cell simulations of HHG on plasma mirrors, in the CWE regime, with and without WFR, in interaction conditions typical of our experiment.

In these simulations, the plasma has a maximum density of  $200n_c$  (corresponding to a maximum

plasma frequency of  $14\omega_0$ , with  $\omega_0$  the laser frequency), an initial density gradient of  $\lambda_L/70$  (with  $\lambda_L$  the laser wavelength), an initial electronic temperature of 0.1 keV, and mobile ions. The laser field has an incidence angle of  $45^\circ$  and is  $p$ -polarized. This field is injected in the simulation box through boundary conditions, in the form of Eq. (2) of Ref. 10, such that it is possible to introduce a controlled amount of wavefront rotation at focus. The laser intensity on target is  $7 \times 10^{17} \text{ W/cm}^2$ . The total electromagnetic field right after the target, obtained by PIC simulations, is then post-processed to be propagated over arbitrary distances, by using a plane waves decomposition.

Figure S3a corresponds to a case without wavefront rotation and a Fourier-Transform limited pulse duration of 5 fs, while Fig. S3b corresponds to the case of maximum wavefront rotation velocity at focus, with the same spectral bandwidth as the previous case, leading to an increased pulse duration of  $\sqrt{2} \times 5 \approx 7 \text{ fs}$  on target. By comparing these two simulations, it is clear that the introduction of wavefront rotation leads to the same spatial and spectral effects as those observed in the experiment. These simulations then make it possible to directly observe the effects that are induced in the time domain, and to confirm that isolated attosecond pulses are indeed generated in our experiment.

In the case without wavefront rotation a short train of three main attosecond pulses is observed, as expected, with all pulses propagating in the same direction. This leads to a smooth Gaussian-like spatial profile of the EUV beam in the far-field. Due to the spectral interferences between these multiple pulses, the obtained EUV spectrum consists of a strongly-modulated, harmonic-like spectrum. When wavefront rotation is introduced, three main attosecond pulses are still observed, which are hardly modified from the standard temporal duration without wavefront rotation. However, these pulses now propagate in different directions, and become spatially separated in the far-field (*i.e.* at distances from the target larger than the Rayleigh length for the corresponding EUV frequencies). As a result, the spatial profile of the resulting EUV beam consists of three slightly overlapping beamlets. Due to this spatial separation, the harmonic-like modulations observed in the EUV spectrum in the absence of wavefront rotation are eliminated, and a continuous spectrum is observed that corresponds with the central attosecond peak from the sheared pulse train.

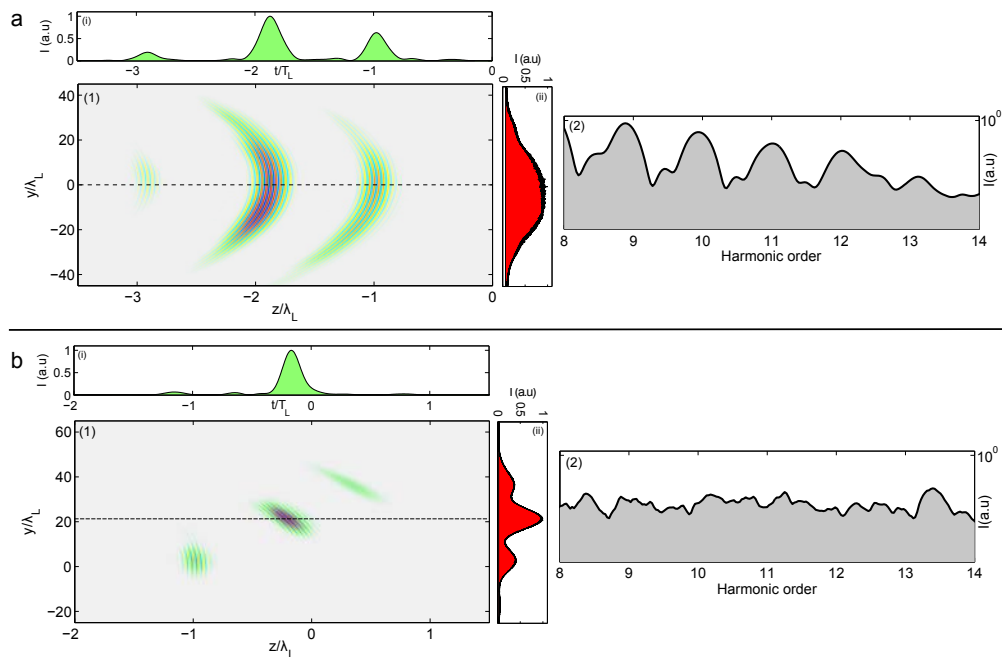


**Figure S3: PIC simulations for attosecond lighthouse effect.** Panel **a** corresponds to the case without WFR, while in panel **b**, WFR has been introduced. In both cases, the central color plot **(1)** displays the  $E$ -field obtained by filtering the reflected radiation between harmonics 11 and 14. This field is plotted as a function of the spatial coordinates  $z$  (propagation direction) and  $y$  (transverse direction), after the pulses have propagated away from the target a distance of  $1400\lambda_L$ —large compared to the Rayleigh length of the EUV radiation. The panels to the right **(ii)** show the temporally-integrated spatial profile of the frequency-filtered radiation, while the upper panels **(i)** display a lineout of the longitudinal intensity profile (equivalent to a temporal profile), at a given position  $y$  in the beam, and corresponding to the intensity derived from the  $E$ -field at the horizontal dashed line. The rightmost graphs **(2)** in **a** and **b** show the spectrum of the emission, spatially-averaged over the entire EUV beam in case **a**, and only over the central beamlet in case **b**.

## S4 Supplementary Movie

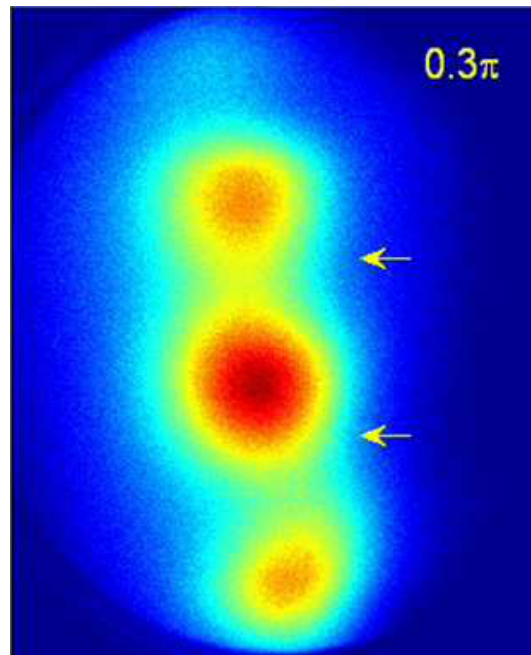


**Figure S4: Demonstration of CEP control.** Screenshot from movie showing effects of changing the laser CEP on the EUV beamlet profile. Each frame shows the EUV beamlet profile as the CEP is changed with a stepsize of  $\pi/10$ . The relative change is displayed in the upper right corner starting from an arbitrary absolute value. The arrows are reference markers introduced as an aid in visualizing the progression of the individual peaks. As in Fig. 4 of the paper, the WFR maps the time progression downward on the figure so that features produced at earlier times in the infrared pulse arrive at the top of the image while later times fall below.